Cluster formations in deformed states for ^{28}Si and ^{32}S

Takatoshi Ichikawa,[1] Yoshiko Kanada-En'yo,[2] and Peter Möller[3]

[1]*Yukawa Institute for Theoretical Physics, Kyoto University, Kyoto 606-8502, Japan*
[2]*Department of Physics, Kyoto University, Kyoto 606-8502, Japan*
[3]*Theoretical Division, Los Alamos National Laboratory, Los Alamos, New Mexico 87545, USA*

We study cluster formation in strongly deformed states for ^{28}Si and ^{32}S using a macroscopic-microscopic model. The study is based on calculated total-energy surfaces, which are the sums of deformation-dependent macroscopic-microscopic potential-energy surfaces and rotational-energy contributions. We analyze the angular-momentum-dependent total-energy surfaces and identify the normal- and superdeformed states in ^{28}Si and ^{32}S. We show that at sufficiently high angular momenta strongly deformed minima appear. The corresponding microscopic density distributions show cluster structures that closely resemble the ^{16}O + ^{12}C and ^{16}O + ^{16}O configurations. At still higher deformations, beyond the minima, valleys develop in the calculated surfaces. These valleys lead to mass divisions that correspond to the target-projectile configurations for which molecular resonance states have been observed. We discuss the relation between the one-body deformed minima and the two-body molecular-resonance states.

A rich variety of nuclear structure data in the *s-d* shell region provides an excellent opportunity to investigate how a system transitions between one-body-like mean-field and two-body-like cluster structures [1,2]. Because of recent progress in experimental techniques, it has been possible to determine that strongly deformed states exist in ^{36}Ar and ^{40}Ca by the observation of γ-ray cascades typical of rotational bands [3,4]. These bands are called superdeformed (SD) bands. Such new data have triggered renewed interest in whether the strongly deformed states exist in other *s-d* shell nuclei.

In this connection, the existence of such states in ^{28}Si and ^{32}S has been theoretically suggested [5–8]. Many experimental searches for and studies of such states have been performed [9,10]. An important feature of nuclear structure in the *s-d* shell region is that the densities of strongly deformed one-body states often exhibit significant cluster structure [11,12], similar to the ^{16}O + ^{16}O configuration suggested to exist in ^{32}S [7,13,14]. Recently, the existence of α-cluster states in ^{32}S was clearly shown in elastic ^{28}Si + α scattering experiments [10]. However, the existence of the strongly deformed states and the mechanism of the cluster formations in ^{28}Si and ^{32}S have not yet been well established.

Another important observation is the molecular resonances emerging just below the Coulomb barrier in the two-body entrance channel in both the ^{16}O + ^{12}C and ^{16}O + ^{16}O reactions, leading to ^{28}Si and ^{32}S, respectively. That is, the molecular-resonance states would consist of the ^{16}O + ^{12}C and ^{16}O + ^{16}O cluster components, similar to the clusters in the strongly deformed states in ^{28}Si and ^{32}S. It is thus interesting to investigate the relation between the one-body deformed states and the two-body molecular-resonance states and the association with the cluster formations in the deformed states.

Two different theoretical approaches have been used to describe the deformed states in the *s-d* shell nuclei. One is nuclear structure calculations using one-body wave functions. Leander and Larsson identified several distinct minima with exotic shapes using the macroscopic-microscopic model [15].

Minima at high angular momenta were also investigated based on a cranking model for the rotational inertia [16]. However, the ℓ^2 term in their mean-field potential leads to many unphysical minima at large deformations. Moreover, strongly necked-in shapes are not possible in the Nilsson perturbed-spheroid (ϵ) parametrization.

The SD states and the low-lying excited states have also been treated in Hartree-Fock-type (HF) self-consistent mean-field calculations [5,19], often coupled with the generator-coordinate method (GCM) [20,21]. For ^{32}S, Kimura and Horiuchi suggested the existence of an SD band containing the ^{16}O + ^{16}O cluster components based on the antisymmetrized molecular dynamics coupled with GCM [7]. They also showed that a third rotational band with $N = 28$, where N is the principal quantum number of the relative motion between clusters, in the ^{16}O + ^{16}O configuration connects to the molecular-resonance states. The existence of the normal-deformed (ND) state in ^{28}Si and its relation to the ^{16}C + ^{12}O molecular resonances were also investigated [8,22].

The second approach is reaction calculations using a two-body potential model appropriate to the entrance channel. Those studies are mainly based on an optical potential that reproduces well the experimental elastic or inelastic cross sections [14,23–27]. For ^{32}S, Ohkubo and Yamashita [14] calculated the SD bands with the deep ^{16}O-^{16}O potential [14]. They identified three rotational bands with $N = 24$, 26, and 28 and showed that the lowest and the third bands correspond to the SD band and the molecular resonances, respectively. Kocak *et al.* also obtained a similar SD band with $N = 24$ using the α-α double-folding potential [28].

The aim of this paper is to show cluster formations in the strongly deformed states for ^{28}Si and ^{32}S. We find that consideration of rotational contributions to the energy is essential. In this study, we apply for the first time the macroscopic-microscopic model, which is very successful in the description of fusion and fission reactions in heavy-mass systems [17,29–32] to very light nuclei. The model allows us to

describe both one-center deformed and two-center cluster-like configurations with mass asymmetry within the same model framework. In this approach the clusters are joined by a neck region with a lower single-particle density. For lighter-mass systems, such treatments are essential for a unified description of the whole process because the scission-point shape closely resembles that of the saddle point, as has been well established in fusion-fission processes below the Businaro-Gallone point [18]. We calculate and analyze total-energy surfaces, which are the sums of a potential-energy surface and a rotational-energy contribution, which are both functions of five shape degrees of freedom. We use the immersion technique to identify reaction channels that we expect correspond to molecular resonances including various mass asymmetric divisions. We show that in this model minima with density distributions corresponding to the cluster configurations of $^{16}O + {}^{12}C$ and $^{16}O + {}^{16}O$ appear at high angular momenta.

We use the three-quadratic-surface (3QS) parametrization [31,32] to describe nuclear shapes in a five-dimensional deformation space. The shape degrees of freedom are a quadrupole-moment parameter Q_2, a neck-related parameter η, left- and right-fragment deformation parameters, ϵ_{f1} and ϵ_{f2}, and a mass-asymmetry parameter α_g. The parameter η describes the curvature of the middle body. The parameter ϵ is the Nilsson perturbed-spheroid parameter. Near scission we have to a very good approximation $\alpha_g = (M_1 - M_2)/(M_1 + M_2)$, where M_1 and M_2 are the masses of the left and right nascent fragments, respectively. The microscopic single-particle potential is calculated by folding a Yukawa function over the shape or "sharp-surface generating volume" [29].

We calculate the adiabatic one-body potential-energy surface in a five-dimensional deformation space for ^{28}Si and ^{32}S and and analyze their structure using the immersion method. Details of the model are given in Ref. [17]. The parameters of the potential-energy model, often referred to as FRLDM (finite-range liquid-drop model) are those of the latest version, FRLDM(2002) [33]. We calculate the potential energies at $41 \times 15 \times 15 \times 15 \times 35$ grid points for Q_2, η, ϵ_{f1}, ϵ_{f2}, and α_g, respectively. For α_g grid points we use $-0.025(0.025)0.825$; the fragment shape grid points are the same as in Ref. [17]; in η the choice is similar. We take into account the shape dependence of the A^0 and Wigner terms in our calculations [34]. However, in the form introduced in our model the Wigner energy is zero for the $N = Z$ nuclei we consider here. Near the ground states, we perform β-constrained calculations, which describe better one-body shapes for small deviations from spherical shape. For the purpose of comparing with calculations in other shape parametrizations we sometimes give the deformations of our shapes in terms of the β shape parameters, obtained by expanding the 3QS shapes in spherical harmonics [30]. We calculate nuclear density distributions and determine the number of nucleons in the left and right fragments by integrating the single-particle densities [35].

Figures 1 and 2 show the calculated results for ^{28}Si and ^{32}S as "optimal" one-dimensional potential-energy curves embedded in the five-dimensional space versus the quadrupole moment. Nuclear densities at points of special interest are also given. The calculated potential-energy curves for ^{28}Si and ^{32}S are quite similar to other calculations [5,7,8,19–21]. At larger
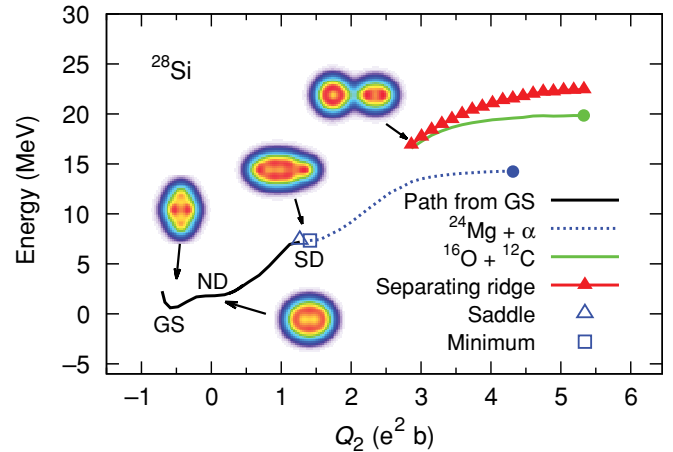

FIG. 1. (Color online) Potential-energy curves for ^{28}Si versus the quadrupole moment. The open square and SD denote the superdeformed minimum. The absolute minimum is denoted by GS. The solid line denotes the potential versus Q_2 near the ground state, along a trajectory that locally minimizes the energy. The gray (green) and dotted lines denote the only relatively prominent valleys found in the one-body potential-energy surface. They correspond to shapes with asymmetries similar to the $^{16}O + {}^{12}C$ and $^{24}Mg + \alpha$ reaction channels. The solid line with superimposed triangles is the ridge separating these two channels.

Q_2, valley-like structures appear in the 5D surface; we show curves corresponding to the bottom of the only two relatively prominent, that is, deep and persistent, valleys we identify. The scission points in each reaction channel are denoted by solid circles. The one-body ground state connects continuously to these two-body cluster channels.

For ^{28}Si, we identify two paths: one given by the dotted line, leading to the $^{24}Mg + \alpha$ reaction channel, and a second given by the gray (green) line, leading to $^{16}O + {}^{12}C$ reaction channel. Those are separated by a potential ridge, shown as a solid
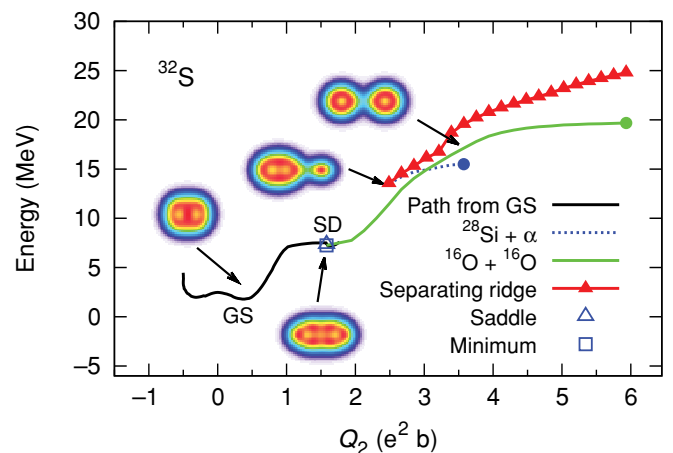

FIG. 2. (Color online) Potential-energy curve for ^{32}S versus the quadrupole moment. The gray (green) and dotted lines are valleys in the one-body potential energy surface corresponding to strongly necked-in one-body shapes with asymmetries similar to those of the $^{16}O + {}^{16}O$ and $^{28}Si + \alpha$ reaction channels. The other symbols are the same as in Fig. 1.

line with superimposed triangles. The calculated ground-state shape is oblate with $Q_2 = -0.59$ (e^2b). We obtain a flat potential-energy curve near $Q_2 = 0.05$ (e^2b), which is consistent with the HF calculation of Ref. [19]. Although this flat area corresponds to a much smaller β than the $\beta_2 \sim 0.5$ of the ND minimum found in Ref. [8], we label this flat part at $Q_2 = 0.05$ (e^2b) ND. For higher angular momenta it evolves into a more well-localized minimum. We furthermore identify the additional energy minimum at $Q_2 = 1.41$ (e^2b) at $\beta = 0.68$, denoted by the open square, with the SD minimum [8]. In spherical shell-model terminology this is interpreted as a $4p$-$16h$ ($4\hbar\omega$) state with the intruder single-particle orbital of $1/2[330]$ (labeled with the Nilsson asymptotic quantum numbers $\Omega^\pi[Nn_z\Lambda]$) at the Fermi energy for both protons and neutrons. From our *deformed* mean-field model point of view, there are no particle-hole excitations since this is the lowest possible energy at this deformation. In this sense, our calculated results and those at $J^\pi = 0^+$ of Ref. [8] are quite similar to each other, both as relates to the shape configurations at the ground-state, the ND, and the SD minima and to the single particle configurations (see Figs. 2(a)–2(c), 4(a), and 4(b) in Ref [8]). The optimal potential-energy curves obtained by [8] for the ^{24}Mg + α and ^{16}O + ^{12}C channels in ^{28}Si are also quite similar to the results here.

For ^{32}S, we identify two paths, one leading to the ^{16}O + ^{16}O [the gray (green) line] the reaction channel and the other leading to the ^{28}Si + α (the dotted line) reaction channel, and the separating ridge (the solid line with the filled triangles). The calculated ground state is prolate with $Q_2 = 0.39$ (e^2b), corresponding to $\beta_2 = 0.24$. We also obtain an additional, almost symmetric, minimum at $Q_2 = 1.58$ (e^2b), corresponding to $\beta = 0.72$, denoted by an open square. This minimum is the SD state. Again, in spherical shell-model terminology this is interpreted as a $4p$-$12h$ ($4\hbar\omega$) state with the intruder single-particle orbital $1/2[330]$ at the Fermi energy for both protons and neutrons.

We now calculate the total energy versus angular momentum (and Q_2) for ^{28}Si and ^{32}S. We calculate the macroscopic rigid-body moment of inertia for the shapes of interest and obtain the total energy by adding the shape-dependent rotational energy to the five-dimensional potential-energy surface. The rotational energy E_R is then given by $E_R = \hbar^2 I(I+1)/2\mathcal{J}_\perp$, where I denotes the collective rotational angular momentum in the intrinsic frame and $\mathcal{J}_\perp$ denotes the rotational moment of inertia. We only consider rotations around the ρ axis, which is perpendicular to the symmetry axis (z axis) [36]. Even if the two fragments are well separated, we treat such configurations as rigid-body rotors. We analyze the total-energy surfaces obtained at each I, using the immersion method.

Figures 3 and 4 show total-energy curves for three different angular momenta along one-dimensional "minimal-energy" paths embedded in the five-dimensional deformation space for ^{28}Si and ^{32}S, respectively. The ND and SD minima are present for ^{28}Si, and the SD minimum is present for ^{32}S. In Figs. 3 and 4, the ND and SD minima at each I are indicated by open squares. The dotted lines through these minima are the optimal pathways from ground-state-like shapes to the ^{24}Mg + α and ^{28}Si + α channels. The other symbols are the same as in Figs. 1 and 2. Nuclear densities at points of special interest are also
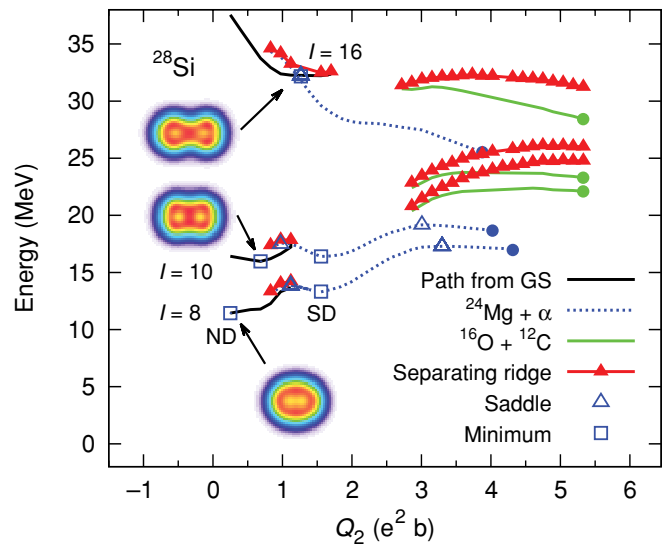

FIG. 3. (Color online) Potential-energy curves versus quadrupole moment for $I = 8$, 10, and 16 for ^{28}Si. The shape configuration of the ND minimum changes to a ^{16}O + ^{12}C cluster-like configuration at $I = 10$. The symbols are the same as in Fig. 1.

given. The potential pockets at the ND minima vanish as the angular momentum increases.

Figure 5 shows the calculated rotational bands in the ND and SD minima. In Fig. 5, the total energies at the ND and SD minima are denoted by solid lines with open squares. For comparison, we plot experimental data as solid squares. However, experimental band assignments have not been well confirmed, except for the ND state of ^{28}Si and the α-cluster states of ^{32}S.

For the ND state of ^{28}Si, the band assignments have been confirmed by γ-ray measurements [37]. We thus directly compare our calculated results with those data. In the top
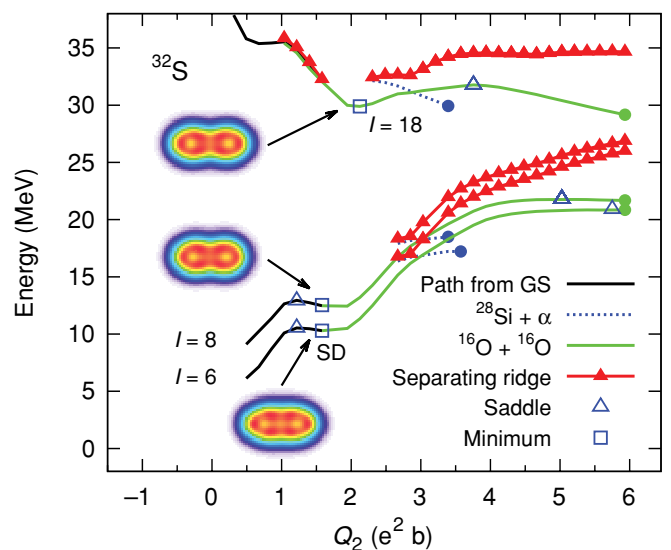

FIG. 4. (Color online) Potential-energy curves at angular momentum $I = 6, 8$, and 18 for ^{32}S versus the quadrupole moment. The shape configuration of the SD minimum changes to a ^{16}O + ^{16}O cluster-like configuration at $I = 8$. The symbols are the same as Fig. 2.
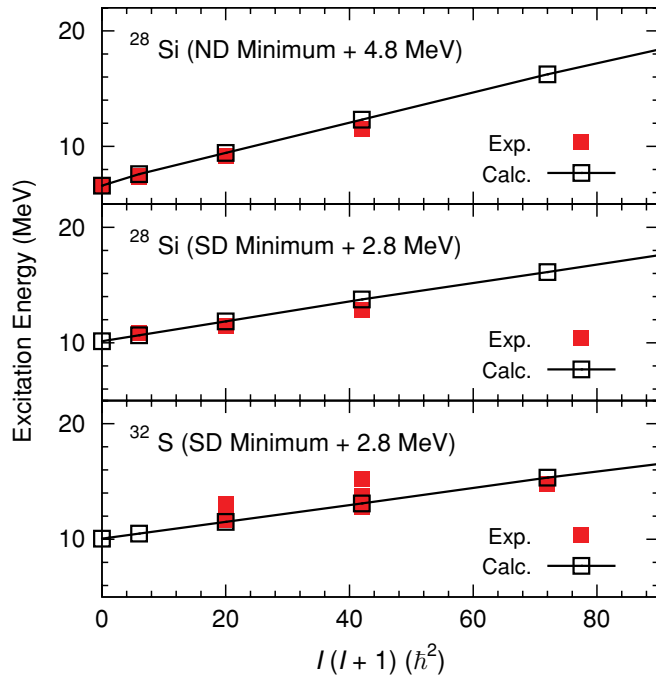
FIG. 5. (Color online) Rotational levels in the ND and SD minima versus the angular momentum I for ^{28}Si and ^{32}S. The solid line with open squares denotes the total energies at the ND or SD minima. The solid squares denote experimental data taken from Refs. [13,39]. We normalize the calculated bandhead energies to experimental data by shifting the ND minimum for ^{28}Si by +4.8 MeV and the SD minima for ^{28}Si and ^{32}S by +2.8 MeV.

panel of Fig. 5, we normalize the calculated bandhead energies to the lowest levels of the experimental data because our calculated energies show some discrepancy with respect to the experimental data. After this normalization, the calculated level spacings agree well with the data, which suggests that the calculated deformation of the ND minimum is realistic. In comparison to other calculations, we find that our calculated rotational bands of the ND state for ^{28}Si correspond to those with the lowest N, namely, $N = 18$ in Refs. [22,27].

The α-cluster states of ^{32}S were recently clearly identified in ^{24}Mg + α elastic-scattering experiments. However, we do not identify minima corresponding to those states in our calculations. The experimentally deduced moment of inertia for those states is about 2 times as large as our calculated results of the SD states (see the bottom panel of Fig. 5), indicating that it is necessary to take into account rotations at smaller Q_2 than in the present calculations in order to reproduce this experimental result. At such small Q_2, triaxial deformations are important. To access triaxial shapes, a model extension such as Ref. [17,38] is necessary. After such an extension, the Jacobi shape transitions in the β-γ deformation space, as shown in Ref. [9], could be studied.

The rotational bands for the SD states of ^{28}Si and ^{32}S have not yet been confirmed. Therefore, we are limited to plotting possible candidates proposed by Refs. [13,39] for those states. The middle and bottom panels of Fig. 5 show the calculated results. In Fig. 5, we also perform the same normalization as for the ND state of ^{28}Si to the experimental results. We consider

that our calculated result for the SD state of ^{32}S corresponds to that with $N = 24$ of Refs. [7,14,28]. After the normalizations, we see that the behaviors of the calculated results for the SD states of both ^{28}Si and ^{32}S are similar to the experimental moment of inertia proposed by Refs. [13,39]. However, further experimental investigations are necessary for establishing the existence of the SD states and for band assignment.

At high angular momentum, the asymmetry at the shape configurations of the ND and SD minima for ^{28}Si and ^{32}S become close to the ^{16}O + ^{12}C and ^{16}O + ^{16}O divisions, respectively. In Figs. 3 and 4, we can clearly see drastic shape transitions, that is, from densities with one center to two-center cluster-like configurations. For the ND and SD minima for ^{28}Si and ^{32}S, the neck formation occurs suddenly at $I = 10$ and 8, respectively.

There are two important mechanisms for such clusterization: (i) intersection between a high-Ω level, whose energy increases with deformation and is mainly localized in the "equator" region, and a low-Ω level, whose energy decreases with deformation (intruder level) and is mainly localized in the "polar" regions, and (ii) mixing of single-particle levels with high quantum number. The former can be seen in the shape transition of the ND minimum for ^{28}Si. At $I = 0$, the neutron level at the Fermi surface consists mainly of the $5/2^+$[202] (98%) state [Fig. 6(a)], which forms the surface of the middle body part in the total density. At $I = 10$, a transition occurs between this last occupied level and the intruder level, which is an admixture of $1/2^+$[211] (75.3%) and [220] (16.4%) and which now becomes the highest occupied level, as shown in Fig. 6(b). In this case, the wave-function density shifts from the surface of the middle body into the two nascent fragments. Mechanism (ii) is at play in the SD minimum for ^{32}S. At $I = 0$, the neutron single particle at the seventh level consists of the $1/2^-$[101] (96.0%) component [Fig. 6(c)]. At $I = 8$, the components of [321] are slightly mixed in this level. The single-particle density of the middle body becomes low due to $1/2^-$[101] (93.2%) and [321] (4.3%), as shown in Fig. 6(d). The component of [321] describes stretching of
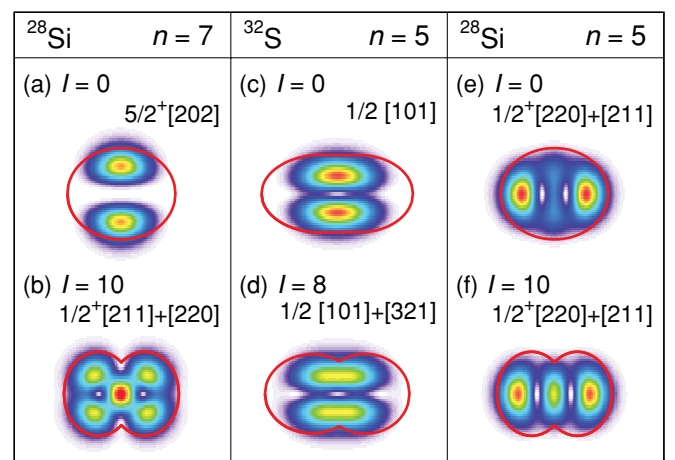

^{28}Si $\quad n = 7$	^{32}S $\quad n = 5$	^{28}Si $\quad n = 5$
(a) $I = 0$ $\quad 5/2^+$[202]	(c) $I = 0$ $\quad 1/2$ [101]	(e) $I = 0$ $\quad 1/2^+$[220]+[211]
(b) $I = 10$ $\quad 1/2^+$[211]+[220]	(d) $I = 8$ $\quad 1/2$ [101]+[321]	(f) $I = 10$ $\quad 1/2^+$[220]+[211]

FIG. 6. (Color online) Density distributions of neutron single-particle wave functions for ^{28}Si and ^{32}S. The solid line denotes the half depth of the mean-field potential. We normalize the color to the density distribution at the maximum of each plot at $I = 0$.

the single-particle densities, and [321] is strongly fragmented into many of the levels in both ^{28}Si and ^{32}S.

The other interesting behavior of the single-particle wave function that influences the clusterization is the neck formation. The neutron single-particle wave function of the fifth level in ^{28}Si consists of the $1/2^+$[220] (66.9%) and [211] (26.8%) components [Fig. 6(e)]. With increasing angular momentum, the [220] component increases, whereas the [211] component decreases, which forms the neck part between two fragments. At $I = 10$, the wave function is described by $1/2^+$[220] (80.3%) and [211] (17%), as shown in Fig. 6(f). This trend can be also seen in the [220] component for ^{32}S. Although it seems that the two fragments are well separated at high angular momentum, they are tightly bonded by the neck formation.

In more elaborate microscopic calculations, the lowest level $J = 0^+$ would contain components of intrinsic states with different I. The highest J is limited to what is obtained when all the spins are aligned, although the potential pocket still exists at high I. In this respect, the obtained density distribution at the ND minimum of $I = 10$ for ^{28}Si is very similar to that at $J = 0^+$ of Ref. [8]. Consequently, the ND and SD states can contain cluster components even at $J = 0^+$.

Our calculations show a plausible mechanism for the origin of the molecular resonances. In the calculations, we can identify the potential valleys leading to the ^{24}Mg + α and ^{16}O + ^{12}C channels in ^{28}Si and to ^{28}Si + α and ^{16}O + ^{16}O channels in ^{32}S, as shown in Figs. 1 and 2. Also, in this study we cannot clearly identify any other valleys and associated density clusters in the potential surface. Consequently, there is an interesting correspondence between the valley structures obtained in our calculations and the observed reaction channels associated with molecular resonances. Expressed differently, we could say that, when entrance-channel target/projectile mass ratios are similar to the one-body density clusters corresponding to the calculated valleys in the potential-energy surfaces, we experimentally observe molecular resonances.

As shown in this study, the highly excited SD and ND states for ^{28}Si and ^{32}S contain significant ^{16}O + ^{12}C and ^{16}O + ^{16}O cluster components, respectively. We expect that those two states relate to the observed molecular resonances because their mass asymmetry at high angular momentum are very close to the target-projectile combinations in the entrance channel for which molecular resonances are observed. It is thus interesting to investigate how those states in the one-body system relate to the molecular resonances in the two-body reaction channels.

A key question is whether the molecular resonances arise because of effects in (1) the final stages of the two-body heavy-ion collision, (2) during formation of the compound system, that is at the top of the fusion barrier, or (3) after formation of a single pre-compound system. The molecular resonances emerge just below the Coulomb barrier in the two-body reaction channels, indicating that those states exist in the region of slightly overlapping densities of colliding two nuclei. It is thus unclear whether those two nuclei are strongly or weakly coupled to each other, corresponding to the one-body "sticking" or the two-body "freely rotating" limits [40], respectively. To investigate those two limits, we calculate the Coulomb barrier heights of the freely rotating

and sticking limits and investigate the correlation between those and the molecular-resonance states.

For the freely rotating limit, we calculate the Coulomb-barrier heights as a function of the orbital angular momentum I for the ^{16}O + ^{12}C and ^{16}O + ^{16}O reactions. In the calculation, we use the Yukawa-plus-exponential model, which is the same framework as used in the present calculations of the potential-energy surface and is well tested in many two-body reactions [41,42]. The Coulomb interaction energy is calculated for two point charges. The centrifugal potential is $\hbar^2 I(I + 1)/2\mu r^2$, where μ is the reduced mass and r is the center-of-mass distance between colliding nuclei. That is, the moment of inertia in the two-body system $\mathcal{J}_{(2bd)}$ is given by $\mathcal{J}_{(2bd)} = \mu r^2$, corresponding to the rotational energy of two freely rotating rigid bodies. When the fusion barrier does not go over a maximum during the approach of the two colliding heavy ions, that is, it keeps rising until touching, we follow conventional practice and define the "Coulomb barrier" as the energy at touching. In the sticking limit, the Coulomb-barrier heights correspond to that of the saddle point in the calculated one-body potential-energy surface.

Figure 7 shows the resulting Coulomb-barrier heights measured relative to two infinitely separated nuclei (the solid
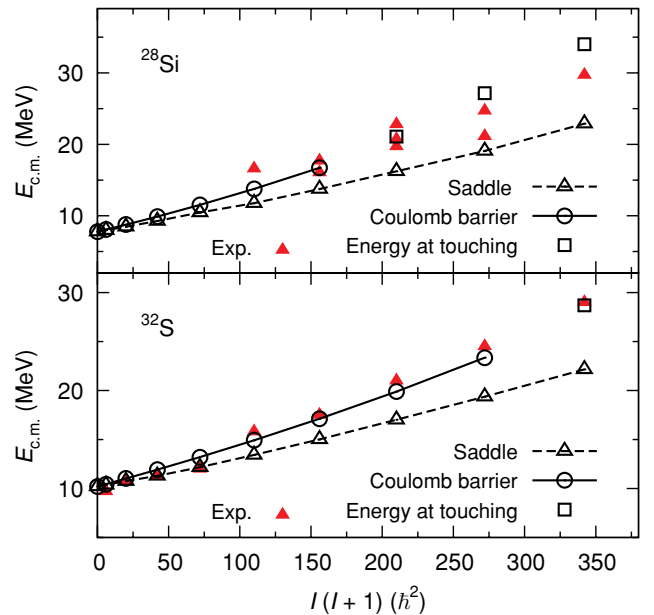

FIG. 7. (Color online) Heights of the Coulomb barrier versus the angular momentum in (top) the ^{16}O + ^{12}C and (bottom) the ^{16}O + ^{16}O reactions. The potential energy is given relative to that of the two infinitely separated nuclei. The solid line with the circles denotes the calculated heights of the Coulomb barrier. The open squares denote the energy at the touching point when the potential pocket in the fusion barrier vanishes. The solid triangles denote the average energies of experimental data for the molecular-resonance states at each angular momentum taken from Refs. [14,27]. The dashed line with the open triangles denotes the heights of the saddle points leading to the ^{16}O + ^{12}C and ^{16}O + ^{16}O reaction channels in the calculated potential-energy surface for ^{28}Si and ^{32}S, respectively. The calculated heights of the saddle points are shifted to fit to the Coulomb-barrier height at $I = 0$.

line with open circles). The energy at the touching point is denoted by the open squares. The average energies of experimental data at each ℓ for the molecular-resonance states tabulated in Refs. [14,27] are denoted by solid triangles. For comparison, we also plot the height of the saddle points leading to the ^{16}O + ^{12}C and ^{16}O + ^{16}O reaction channels in the calculated potential-energy surface for ^{28}Si and ^{32}S (the dashed line with open triangles). We shift the calculated height of the saddle points to fit to the Coulomb-barrier height of the two-body reactions at $I = 0$ because we focus here on discussing their moments of inertia, not their absolute energies.

In Fig. 7, we can clearly see the calculated Coulomb-barrier heights strongly correlate with the experimental data of the molecular-resonance states, whereas the slope of the height of the saddle points differs from those. The moment of inertia for the molecular-resonance states is well reproduced by the freely rotating $\mathcal{J}_{(2bd)}$, rather than the one-body ridged rotor $\mathcal{J}_{\perp}$, indicating that the molecular resonances are governed by effects in the two-body entrance channel.

In the deformed states, the two clusters show the property of the one-body ridged rotor, as shown in Fig. 5, whereas in the molecular-resonance states, they can freely rotate. The former comes from the single-particle wave functions tightly bonding two clusters, as shown in Figs. 6(b) and 6(f). That is, the one-body ridged rotor would change to the two-body freely rotating rotor if such bonding wave functions of the neck part vanished with the development of two clearly separated clusters. Such wave functions thus play an important role in transitioning from the one-body deformed state to the two-body molecular-resonance states.

In summary, we have investigated cluster formation in the one-body ND and SD states for ^{28}Si and ^{32}S and its relation to the molecular-resonance states. Our study is based on total-energy surfaces calculated in a five-dimensional deformation space. The total energy is the sum of a potential-energy and a rotational-energy contribution. The total-energy surfaces are analyzed as functions of angular momentum. We identified the ND and SD minima in the potential-energy surface for ^{28}Si and ^{32}S. The obtained deformed minima are quite similar to those proposed by other theoretical models. The level spacings of the rotational bands for those deformed minima are in good agreement with the experimental data. The nuclear densities in the ND and SD minima become very cluster-like when the angular momentum reaches $I = 8$ and 10, respectively. We show how cluster configurations develop due to changing occupation of specific single-particle levels with increasing deformation and angular momentum. When we consider the paths from the one-body ND and SD states to the ^{12}C + ^{16}O and ^{16}O + ^{16}O channels and change the inertia from that of a one-body rigid rotor to that of a freely rotating system for the corresponding two-body reaction channels, we can show that the molecular resonances are connected to the ND and SD states.

[1] P. R. Betts and A. H. Wuosmaa, Rep. Prog. Phys. **60**, 819 (1997).

[2] M. Freer, Rep. Prog. Phys. **70**, 2149 (2007).

[3] C. E. Svensson *et al.*, Phys. Rev. Lett. **85**, 2693 (2000).

[4] E. Ideguchi *et al.*, Phys. Rev. Lett. **87**, 222501 (2001).

[5] M. Yamagami and K. Matsuyanagi, Nucl. Phys. A **672**, 123 (2000).

[6] T. Inakura, S. Mizutori, M. Yamagami, and K. Matsuyanagi, Nucl. Phys. A **710**, 261 (2003).

[7] M. Kimura and H. Horiuchi, Phys. Rev. C **69**, 051304(R) (2004).

[8] Y. Taniguchi, Y. Kanada-En'yo, and M. Kimura, Phys. Rev. C **80**, 044316 (2009).

[9] D. Pandit *et al.*, Phys. Rev. C **81**, 061302(R) (2010).

[10] T. Lönnroth *et al.*, Eur. Phys. J. A **46**, 5 (2010).

[11] H. Horiuchi, in *Clusters in Nuclei*, Lecture Notes in Physics Vol. 818, edited by C. Beck (Springer, Berlin, 2010), Vol. 1, Chap. 2, pp. 57–108.

[12] Y. Kanada-En'yo and M. Kimura, in *Clusters in Nuclei*, Lecture Notes in Physics Vol. 818, edited by C. Beck (Springer, Berlin, 2010), Vol. 1, Chap. 4, pp. 109–128.

[13] K. Morita, S. Kubono, M. H. Tanaka, H. Utsunomiya, M. Sugitani, S. Kato, J. Schimizu, T. Tachikawa, and N. Takahashi, Phys. Rev. Lett. **55**, 185 (1985).

[14] S. Ohkubo and K. Yamashita, Phys. Rev. C **66**, 021301(R) (2002).

[15] G. Leander and S. E. Larsson, Nucl. Phys. A **239**, 93 (1975).

[16] I. Ragnarsson, S. Aberg, and R. K. Sheline, Phys. Scr. **24**, 215 (1981).

[17] P. Möller, A. J. Sierk, T. Ichikawa, A. Iwamoto, R. Bengtsson, H. Uhrenholt, and S. Åberg, Phys. Rev. C **79**, 064304 (2009).

[18] S. J. Sanders, A. Szanto de Toledo, and C. Beck, Phys. Rep. **311**, 487 (1999).

[19] K. Kaneko, T. Mizusaki, Y. Sun, and M. Hasegawa, Phys. Lett. B **679**, 214 (2009).

[20] R. R. Rodríguez-Guzmán, J. L. Egido, and L. M. Robledo, Phys. Rev. C **62**, 054308 (2000).

[21] M. Bender, H. Flocard, and P.-H. Heenen, Phys. Rev. C **68**, 044321 (2003).

[22] Y. Kanada-En'yo, M. Kimura, and H. Horiuchi, Nucl. Phys. A **738**, 3 (2004).

[23] W. Scheid, W. Greiner, and R. Lemmer, Phys. Rev. Lett. **25**, 176 (1970).

[24] M. P. Nicoli *et al.*, Phys. Rev. C **60**, 064608 (1999).

[25] W. von Oertzen, H. G. Bohlen, and D. T. Khoa, Nucl. Phys. A **722**, 202c (2003).

[26] Y. Kondo, B. A. Robson, and R. Smith, Phys. Lett. B **227**, 310 (1989).

[27] S. Ohkubo and K. Yamashita, Phys. Lett. B **578**, 304 (2004).

[28] G. Kocak, M. Karakoc, I. Boztosun, and A. B. Balantekin, Phys. Rev. C **81**, 024615 (2010).

[29] M. Bolsterli, E. O. Fiset, J. R. Nix, and J. L. Norton, Phys. Rev. C **5**, 1050 (1972).

[30] P. Möller, J. R. Nix, W. D. Myers, and W. J. Swiatecki, At. Data Nucl. Data Tables **59**, 185 (1995).

[31] J. R. Nix, University of California Radiation Laboratory Report UCRL-17958, 1968.

[32] J. R. Nix, Nucl. Phys. A **130**, 241 (1969).

[33] P. Möller, A. J. Sierk, and A. Iwamoto, Phys. Rev. Lett. **92**, 072501 (2004).

[34] P. Möller, J. R. Nix, and W. J. Swiatecki, Nucl. Phys. A **492**, 349 (1989).

[35] T. Ichikawa, A. Iwamoto, and P. Möller, Phys. Rev. C **79**, 014305 (2009).

[36] R. W. Hasse and W. D. Myers, *Geometrical Relationships of Macroscopic Nuclear Physics* (Springer-Verlag, Berlin, 1988).

[37] F. Glatz, J. Siefert, P. Betz, E. Bitterwolf, A. Burkard, F. Heidinger, Th. Kern, R. Lehmann, S. Norbert, and H. Röpke, Z. Phys. A **303**, 239 (1981).

[38] P. Möller, A. J. Sierk, R. Bengtsson, H. Sagawa, and T. Ichikawa, At. Data Nucl. Data Tables (to be published).

[39] R. K. Sheline, S. Kubono, K. Morita, and M. H. Tanaka, Phys. Lett. B **119**, 263 (1982).

[40] C. F. Tsang, Phys. Scr. A **10**, 90 (1974).

[41] H. J. Krappe, J. R. Nix, and A. J. Sierk, Phys. Rev. C **20**, 992 (1979).

[42] T. Ichikawa, K. Hagino, and A. Iwamoto, Phys. Rev. C **75**, 057603 (2007); **75**, 064612 (2007); Phys. Rev. Lett. **103**, 202701 (2009).